Aalto University

Aaltodoc

OPEN ACCESS

Author(s):   Tuovinen, Toni & Hinkkanen, Marko

Title: Adaptive Full-Order Observer With High-Frequency Signal Injection for Synchronous Reluctance Motor Drives

Year: 2014

Version: Post print

Adaptive Full-Order Observer With High-Frequency Signal Injection for Synchronous Reluctance Motor Drives

Toni Tuovinen and Marko Hinkkanen, *Senior Member, IEEE*

Abstract—A back-EMF-based position observer for motion-sensorless synchronous reluctance motor drives is augmented with high-frequency signal-injection method for improved low-speed operation. Previously proposed observer structure is further improved to account for the cross saturation in the motor. The combined observer is experimentally evaluated using a 6.7-kW synchronous reluctance motor drive in low-speed operation and under various load conditions. The resulting position error at low speeds and standstill is small.

Index Terms—Observer, parameter uncertainties, speed sensorless, stability conditions.

I. INTRODUCTION

The synchronous reluctance motor (SyRM) has recently re-emerged as a contender to the induction motor in variable-speed drives [1]–[3]. As compared to the permanent-magnet synchronous motor (PMSM), the SyRM is magnetized from the stator winding, which renders field-weakening operation a straightforward procedure. The recent price increase of rare-earth metals has also made the SyRM and permanent-magnet assisted SyRM more favorable in relation to the PMSM.

Position-sensorless operation is commonly preferred. At high speeds, methods based on the back electromotive force (EMF) can be used. Since the SyRM can be seen as a special case of the salient PMSM, back-EMF-based methods suitable for salient PMSMs, for example the observers proposed in [4], [5], can be used for SyRMs with slight modifications.

The back-EMF-based methods fail to estimate the position at low speeds and standstill. As the SyRM is inherently salient, methods for accurate rotor-position estimation even at standstill are readily applicable. These methods can be roughly categorized as 1) signal-injection methods [2], [6]–[9], 2) modified PWM methods [10], [11], and 3) methods based on stator current variation without additional signal [12], [13]. Although some authors favor the usage of signal-injection methods at all speeds [14], it is often desirable to avoid additional noise and losses by using a back-EMF-based position estimation method, combined with a signal-injection method applied only at the lowest speeds [2], [15]–[17].

SyRMs are usually magnetically saturated in the rated operating point. The d-axis flux component saturates strongly

as a function of the corresponding current component. Furthermore, the d-axis saturation is coupled with the q-axis saturation. This cross saturation presents an error in the position estimate obtained from the signal-injection method. Typically, compensation for this estimation error is either omitted or it is carried out by directly correcting the output variable, i.e., the position estimate.

In this paper, an adaptive full-order observer, combined with high-frequency signal injection [4], is applied for a SyRM drive in order to improve low-speed operation. The method is further improved to account for the cross saturation in the motor. Since the information provided by the signal-injection method is utilized via correcting internal states of the underlying full-order observer, the position error caused by the cross saturation has to be compensated for before the additional information is introduced to the underlying observer. Otherwise, the dynamics of the combined observer might be impaired.

A minimum requirement for any observer is that the estimation-error dynamics of the closed-loop system are locally stable at every operating point in ideal conditions. In order to satisfy this requirement and to simplify the tuning procedure, a stabilizing gain proposed in [18] is taken as a starting point. This gain is modified in order to take into account the effect of the signal-injection method on the estimation-error dynamics.

After a review of the motor model in Section II and the rotor-position observers in Section III, the main contributions of the paper are presented Section IV:

1) A modified position estimation method, based on signal injection, which reduces the steady-state estimation error caused by cross saturation, is proposed.
2) A stabilizing gain modification for the combined observer is proposed.

The experimental setup is described in Section V, and the performance of the drive at low speeds and standstill is experimentally validated using a 6.7-kW SyRM drive in Section VI.

II. SyRM MODEL

A. Fundamental-Excitation Model

Real space vectors will be used here. For example, the stator-current vector is $\boldsymbol{i}_\mathrm{s} = [i_\mathrm{d}, i_\mathrm{q}]^\mathrm{T}$, where i_d and i_q are the components of the vector and the matrix transpose is marked with the superscript T.

The electrical position of the d-axis is denoted by ϑ_m. The d-axis is defined as the direction of the maximum inductance of the rotor. The position depends on the electrical angular rotor speed ω_m according to

$$\frac{\mathrm{d}\vartheta_\mathrm{m}}{\mathrm{d}t} = \omega_\mathrm{m}. \tag{1}$$

To simplify the analysis in the following sections, the machine model will be expressed in the *estimated* rotor reference frame, whose d-axis is aligned at $\hat{\vartheta}_\mathrm{m}$ with respect to the stator reference frame. The stator inductance is

$$\boldsymbol{L} = \mathrm{e}^{-\tilde{\vartheta}_\mathrm{m}\mathbf{J}} \begin{bmatrix} L_\mathrm{d} & 0 \\ 0 & L_\mathrm{q} \end{bmatrix} \mathrm{e}^{\tilde{\vartheta}_\mathrm{m}\mathbf{J}} \tag{2}$$

where $\tilde{\vartheta}_\mathrm{m} = \hat{\vartheta}_\mathrm{m} - \vartheta_\mathrm{m}$ is the estimation error in the rotor position, L_d the direct-axis inductance, and L_q the quadrature-axis inductance. The coordinate transformation matrices are expressed using matrix exponential, i.e. $\mathrm{e}^{\tilde{\vartheta}_\mathrm{m}\mathbf{J}} = \cos\tilde{\vartheta}_\mathrm{m}\mathbf{I} + \sin\tilde{\vartheta}_\mathrm{m}\mathbf{J}$, where the identity matrix and the orthogonal rotation matrix are

$$\mathbf{I} = \begin{bmatrix} 1 & 0 \\ 0 & 1 \end{bmatrix}, \quad \mathbf{J} = \begin{bmatrix} 0 & -1 \\ 1 & 0 \end{bmatrix}$$

respectively.

The voltage equation is

$$\frac{\mathrm{d}\boldsymbol{\psi}_\mathrm{s}}{\mathrm{d}t} = \boldsymbol{u}_\mathrm{s} - R_\mathrm{s}\boldsymbol{i}_\mathrm{s} - \hat{\omega}_\mathrm{m}\mathbf{J}\boldsymbol{\psi}_\mathrm{s} \tag{3}$$

where $\boldsymbol{\psi}_\mathrm{s}$ is the stator-flux vector, $\boldsymbol{u}_\mathrm{s}$ the stator-voltage vector, R_s the stator resistance, and $\hat{\omega}_\mathrm{m} = \mathrm{d}\hat{\vartheta}_\mathrm{m}/\mathrm{d}t$ is the angular speed of the coordinate system. The stator current is

$$\boldsymbol{i}_\mathrm{s} = \boldsymbol{L}^{-1}\boldsymbol{\psi}_\mathrm{s} \tag{4}$$

where it is worth noticing that the inductance matrix $\boldsymbol{L}$ depends nonlinearly on the position estimation error $\tilde{\vartheta}_\mathrm{m}$.

B. Saturation Model

The inductances L_d and L_q in (2) depend on the flux components (or the current components) due to magnetic saturation. This dependency has been modeled as [19]

$$L_\mathrm{d}\left(\psi_\mathrm{d}, \psi_\mathrm{q}\right) = \frac{L_\mathrm{du}}{1 + \alpha|\psi_\mathrm{d}|^k + \frac{\delta L_\mathrm{du}}{d+2}|\psi_\mathrm{d}|^m|\psi_\mathrm{q}|^{n+2}} \tag{5a}$$

$$L_\mathrm{q}\left(\psi_\mathrm{d}, \psi_\mathrm{q}\right) = \frac{L_\mathrm{qu}}{1 + \gamma|\psi_\mathrm{q}|^l + \frac{\delta L_\mathrm{qu}}{c+2}|\psi_\mathrm{d}|^{m+2}|\psi_\mathrm{q}|^n} \tag{5b}$$

where all parameters $L_\mathrm{du}, L_\mathrm{qu}, \alpha, \gamma, \delta, k, l, m,$ and n should be positive.

C. High-Frequency Model

The incremental inductances seen by high-frequency excitation are

$$L_\mathrm{dd} = \frac{\partial\psi_\mathrm{d}}{\partial i_\mathrm{d}}, \quad L_\mathrm{dq} = \frac{\partial\psi_\mathrm{d}}{\partial i_\mathrm{q}}, \quad L_\mathrm{qd} = \frac{\partial\psi_\mathrm{q}}{\partial i_\mathrm{d}}, \quad L_\mathrm{qq} = \frac{\partial\psi_\mathrm{q}}{\partial i_\mathrm{q}}. \tag{6}$$

Due to reciprocity, $L_\mathrm{qd} = L_\mathrm{dq}$ will be assumed. It is worth noticing that $L_\mathrm{qd} = L_\mathrm{dq} = 0$ would hold in the case of no cross-saturation. Furthermore, if the machine did not saturate at all, $L_\mathrm{dd} = L_\mathrm{d}$ and $L_\mathrm{qq} = L_\mathrm{q}$ would hold.
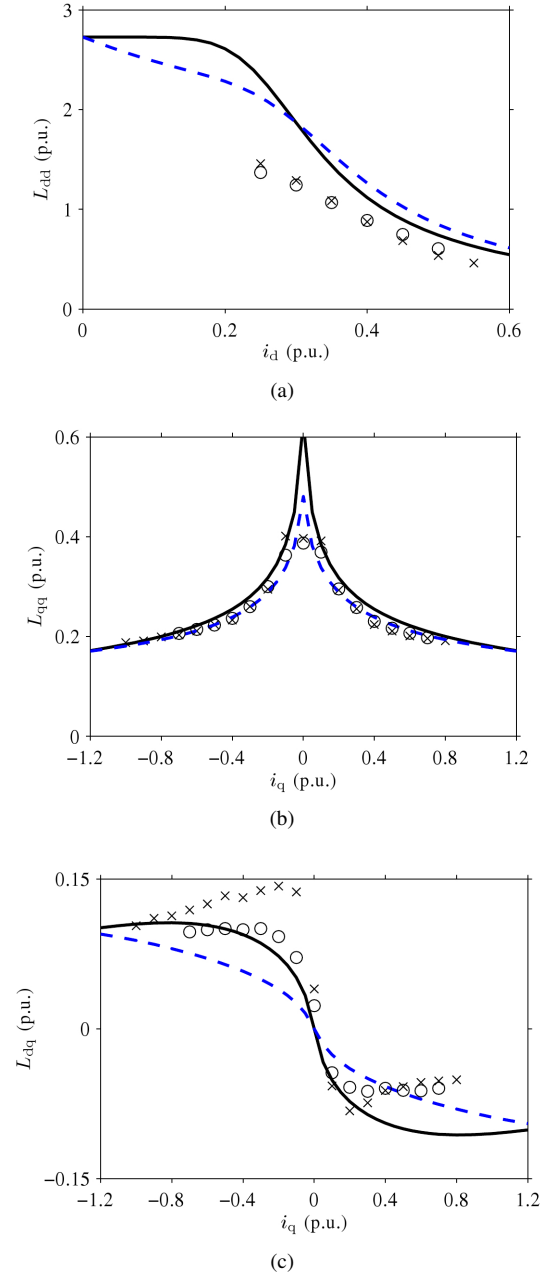

Fig. 1. Incremental inductances as functions of currents for a 6.7-kW SyRM: (a) L_dd as function of i_d for two different values of i_q, (b) L_qq as function of i_q for two different values of i_d, (c) L_dq as function of i_q for two different values of i_d. In (a), the values of i_q are 0 p.u. (solid line, crosses) and 0.75 p.u. (dashed line, circles). In (b) and (c), the values of i_d are 0.3 p.u. (solid line, crosses) and 0.5 p.u. (dashed line, circles). Crosses and circles are measured values, lines are values estimated by the fundamental-excitation model (5).

The incremental inductances seen by the high-frequency excitation do not necessarily coincide with the incremental inductances seen by the fundamental excitation [8]. This is demonstrated in Fig. 1, where the incremental inductances measured using 500 Hz voltage excitation and incremental inductances predicted by the fundamental-excitation model (5) are depicted for a 6.7-kW SyRM (cf. Section V). The saliency ratio of this machine in the rated operating point is approximately $L_\mathrm{d}/L_\mathrm{q} = 6.5$.
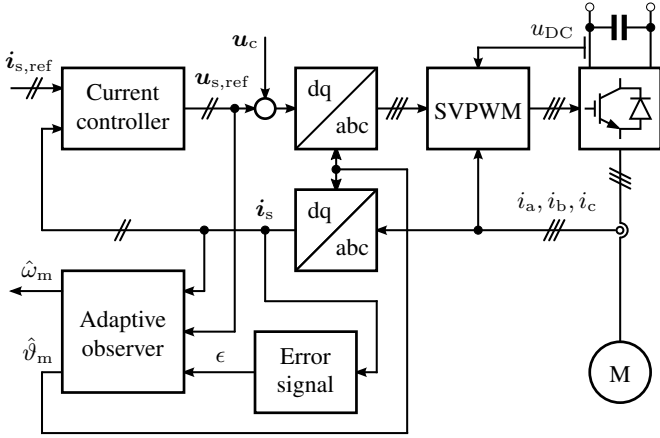
Fig. 2. Block diagram of the vector control system. The DC-link voltage u_{DC} and the phase currents i_a, i_b, and i_c are measured. The high-frequency voltage excitation $\boldsymbol{u}_c = [u_c \cos(\omega_c t), 0]^T$ is superimposed on the voltage reference. Dead-time effect and power-device voltage drops are compensated for in the space-vector modulator (SVPWM) using the phase-current feedback. The contents of the blocks "Adaptive observer" and "Error signal" are shown in Figs. 3(a) and 3(b), respectively.

In Fig. 1(a), the inductance L_{dd} is shown as a function of i_d for two different values of i_q. In Figs. 1(b) and 1(c), the inductances L_{qq} and L_{dq} are shown as functions of i_q for two different values of i_d, respectively. It can be seen that L_{dd} and L_{dq} estimated by the fundamental-excitation model (lines) differ considerably from the measured values (crosses and circles), but the estimated L_{qq} coincides with the measured values with good accuracy. The error between the measured values and predicted values originates from iron losses inflicted by the high-frequency signal injection. If the frequency of the injected signal were increased, the motor would appear less salient and eventually position information from the signal injection would be lost.

III. ROTOR-POSITION OBSERVER

The block diagram of a sensorless vector-controlled SyRM drive is shown in Fig. 2. When the drive is operated in the speed-control mode, the control system is augmented with the speed controller, whose feedback signal is the rotor speed estimate $\hat{\omega}_m$. In the following, the adaptive full-order observer and the error-signal calculation are considered.

A. Adaptive Full-Order Observer

The adaptive full-order observer [4], [20] illustrated in Fig. 3(a) is considered. In the adjustable model, the stator-flux vector and stator-current vector are estimated according to

$$\frac{d\hat{\boldsymbol{\psi}}_s}{dt} = \boldsymbol{u}_s - \hat{R}_s \hat{\boldsymbol{i}}_s - \hat{\omega}_m \mathbf{J} \hat{\boldsymbol{\psi}}_s + \boldsymbol{K} \tilde{\boldsymbol{i}}_s \qquad (7a)$$

$$\hat{\boldsymbol{i}}_s = \hat{\boldsymbol{L}}^{-1} \hat{\boldsymbol{\psi}}_s \qquad (7b)$$

where $\hat{\boldsymbol{i}}_s$ is the estimated stator-current vector, $\tilde{\boldsymbol{i}}_s = \hat{\boldsymbol{i}}_s - \boldsymbol{i}_s$ is the estimation error of the stator current, $\boldsymbol{K}$ is the observer gain matrix, and $\hat{R}_s$ is the model stator resistance. The model inductance matrix is

$$\hat{\boldsymbol{L}} = \begin{bmatrix} \hat{L}_d & 0 \\ 0 & \hat{L}_q \end{bmatrix} \qquad (8)$$
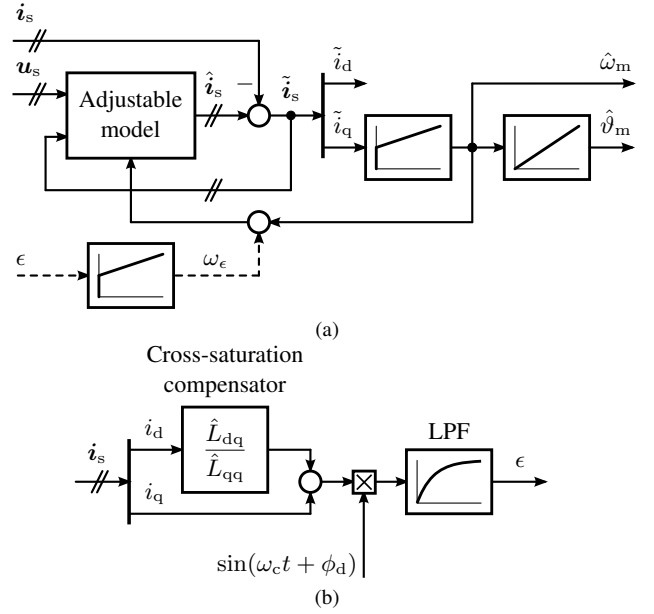

(a)

(b)

Fig. 3. (a) Adaptive observer. The adjustable model is defined in (24), while it reduces to (7) at medium and high speeds. (b) Proposed error-signal calculation scheme. The bandwidth of the first-order low-pass filter (LPF) is α_{lp}. The effect of the discretization delay on the demodulation process is compensated for by means of the constant parameter ϕ_d.

where $\hat{L}_d$ and $\hat{L}_q$ are the direct-axis and quadrature-axis model inductances, respectively. Without loss of generality, the elements of the observer gain matrix are expressed as

$$\boldsymbol{K} = \begin{bmatrix} \hat{R}_s + \hat{L}_d k_{11} & \hat{L}_q k_{12} \\ \hat{L}_d k_{21} & \hat{R}_s + \hat{L}_q k_{22} \end{bmatrix} \qquad (9)$$

in order to simplify the following equations. The four tuning parameters are k_{11}, k_{12}, k_{21}, and k_{22}. The rotor speed is estimated with the proportional-integral (PI) algorithm

$$\hat{\omega}_m = \boldsymbol{k}_p \tilde{\boldsymbol{i}}_s + \boldsymbol{k}_i \int \tilde{\boldsymbol{i}}_s dt. \qquad (10)$$

The gain vectors $\boldsymbol{k}_p$ and $\boldsymbol{k}_i$ are chosen to utilize the estimation error only in the q-axis direction,

$$\boldsymbol{k}_p = [0, k_p], \quad \boldsymbol{k}_i = [0, k_i]. \qquad (11)$$

B. General Stabilizing Gain Design

Locally stable estimation-error dynamics in every operating point are guaranteed for accurate model parameters, if the elements of the observer gain matrix are selected as [18]

$$k_{11} = k'_{11} \qquad (12a)$$
$$k_{12} = -\beta k_{11} \qquad (12b)$$
$$k_{21} = k'_{21} \qquad (12c)$$
$$k_{22} = -\beta k_{21} \qquad (12d)$$

where $\beta = i_q/i_d$ and the functions k'_{11} and k'_{21} are

$$k'_{11} = -\frac{b + \beta(c/\hat{\omega}_m - \omega_m)}{\beta^2 + 1} \qquad (13a)$$

$$k'_{21} = \frac{\beta b - c/\hat{\omega}_m + \hat{\omega}_m}{\beta^2 + 1} \qquad (13b)$$

The new design parameters are b and c and they should be positive. In order to simplify the resulting equations, the gains k_p and k_i are scaled according to [18]

$$k_{\mathrm{p}} = \frac{\hat{L}_{\mathrm{q}}d}{(\hat{L}_{\mathrm{d}} - \hat{L}_{\mathrm{q}})i_{\mathrm{d}}}, \quad k_{\mathrm{i}} = \frac{\hat{L}_{\mathrm{q}}e}{(\hat{L}_{\mathrm{d}} - \hat{L}_{\mathrm{q}})i_{\mathrm{d}}} \qquad (14)$$

where d and e are the new design parameters, which may depend on the rotor speed. With this gain selection, the characteristic polynomial of the closed-loop system consisting of (1) – (4) and (7) – (14) can, after linearization, be split into a product of two second-order polynomials,

$$(s^2 + bs + c)(s^2 + ds + e) \qquad (15)$$

and the stability is guaranteed for all positive values of b, c, d, and e, if the model parameters are accurate. The observer is of the fourth order, and there are four gains. In order to reduce the number of design parameters, d and e can be chosen as [21]

$$d = 2\rho, \quad e = \rho^2 \qquad (16)$$

yielding a double pole located at $s = -\rho$. The remaining three design parameters are b, c, and ρ, which should be positive. In summary, the selected gain formulations in (12) and (14) enable direct placement of the closed-loop observer poles (assuming the linearized system, accurate model parameters, and no correction from the signal-injection method).

C. High-Frequency Signal Injection

As shown in Fig. 2, a high-frequency voltage excitation is superimposed on the stator voltage in the estimated d-axis direction [14],

$$\boldsymbol{u}_{\mathrm{c}} = \begin{bmatrix} u_{\mathrm{c}} \cos(\omega_{\mathrm{c}}t) \\ 0 \end{bmatrix}. \qquad (17)$$

The high-frequency current responses depend on the position error,

$$i_{\mathrm{dc}} = \frac{u_{\mathrm{c}} \sin(\omega_{\mathrm{c}}t)}{\omega_{\mathrm{c}} L_{\mathrm{det}}} \left[L_{\Sigma} - L_{\Delta} \cos(2\tilde{\vartheta}_{\mathrm{m}}) - L_{\mathrm{dq}} \sin(2\tilde{\vartheta}_{\mathrm{m}}) \right] \qquad (18a)$$

$$i_{\mathrm{qc}} = \frac{u_{\mathrm{c}} \sin(\omega_{\mathrm{c}}t)}{\omega_{\mathrm{c}} L_{\mathrm{det}}} \left[L_{\Delta} \sin(2\tilde{\vartheta}_{\mathrm{m}}) - L_{\mathrm{dq}} \cos(2\tilde{\vartheta}_{\mathrm{m}}) \right] \qquad (18b)$$

where

$$L_{\mathrm{det}} = L_{\mathrm{dd}} L_{\mathrm{qq}} - L_{\mathrm{dq}}^2 \qquad (19a)$$

$$L_{\Sigma} = \frac{L_{\mathrm{dd}} + L_{\mathrm{qq}}}{2} \qquad (19b)$$

$$L_{\Delta} = \frac{L_{\mathrm{dd}} - L_{\mathrm{qq}}}{2}. \qquad (19c)$$

Conventionally, only the high-frequency current component perpendicular to the injected signal is used in position estimation, which is then demodulated and low-pass filtered (LPF) [21], [22],

$$\epsilon = \mathrm{LPF}\{i_{\mathrm{q}} \sin(\omega_{\mathrm{c}}t)\}. \qquad (20)$$

This demodulation process corresponds to Fig. 3(b) if only the q-component of the current is used. Using (18) and (20), the resulting quasi-steady-state error signal ϵ can be approximated as

$$\epsilon \approx \frac{u_{\mathrm{c}}}{2\omega_{\mathrm{c}} L_{\mathrm{det}}} \left[L_{\Delta} \sin(2\tilde{\vartheta}_{\mathrm{m}}) - L_{\mathrm{dq}} \cos(2\tilde{\vartheta}_{\mathrm{m}}) \right]. \qquad (21)$$

If this error signal is driven to zero, a nonzero steady-state position error

$$\tilde{\vartheta}_{\mathrm{m0}} = \frac{1}{2} \arctan\left(\frac{L_{\mathrm{dq}}}{L_{\Delta}} \right) \qquad (22)$$

results due to cross saturation [23].

D. Combined Observer

In the combined observer proposed in [4], the error signal ϵ is driven to zero by means of the PI algorithm

$$\omega_{\epsilon} = \gamma_{\mathrm{p}}\epsilon + \gamma_{\mathrm{i}} \int \epsilon \mathrm{d}t. \qquad (23)$$

This correction ω_{ϵ} is combined with the observer (7), resulting in

$$\frac{\mathrm{d}\hat{\boldsymbol{\psi}}_{\mathrm{s}}}{\mathrm{d}t} = \boldsymbol{u}_{\mathrm{s}} - \hat{R}_{\mathrm{s}}\hat{\boldsymbol{i}}_{\mathrm{s}} - (\hat{\omega}_{\mathrm{m}} + \omega_{\epsilon})\mathbf{J}\hat{\boldsymbol{\psi}}_{\mathrm{s}} + \boldsymbol{K}\tilde{\boldsymbol{i}}_{\mathrm{s}}. \qquad (24)$$

The gains in (23) are

$$\gamma_{\mathrm{p}} = \frac{\alpha_{\mathrm{i}}}{k_{\epsilon}}, \quad \gamma_{\mathrm{i}} = \frac{\alpha_{\mathrm{i}}^2}{3k_{\epsilon}}, \qquad (25)$$

where α_{i} is the approximate bandwidth of the PI algorithm and k_{ϵ} is the ideal signal-injection gain from the error signal ϵ to the position error $\tilde{\vartheta}_{\mathrm{m}}$, given by

$$k_{\epsilon} = \frac{u_{\mathrm{c}}}{\omega_{\mathrm{c}}} \frac{\hat{L}_{\mathrm{d}} - \hat{L}_{\mathrm{q}}}{2\hat{L}_{\mathrm{d}}\hat{L}_{\mathrm{q}}}. \qquad (26)$$

A first-order low-pass filter is considered in the demodulation process in (20). The filter bandwidth is selected to be $\alpha_{\mathrm{lp}} = 3\alpha_{\mathrm{i}}$ in accordance with [4].

A smooth transition from standstill to high-speed operation is implemented by decreasing the injected voltage and the bandwidth of the PI algorithm as the speed increases,

$$u_{\mathrm{c}} = u_{\mathrm{c0}}f(\hat{\omega}_{\mathrm{m}}), \quad \alpha_{\mathrm{i}} = \alpha_{\mathrm{i0}}f(\hat{\omega}_{\mathrm{m}}) \qquad (27)$$

where u_{c0} is the amplitude of the injected voltage and α_{i0} is the bandwidth of the PI algorithm at zero speed. The transition function is selected as

$$f(\hat{\omega}_{\mathrm{m}}) = \begin{cases} 1 - \left| \frac{\hat{\omega}_{\mathrm{m}}}{\omega_{\Delta}} \right|, & \text{if } |\hat{\omega}_{\mathrm{m}}| \leq \omega_{\Delta} \\ 0, & \text{otherwise}. \end{cases} \qquad (28)$$

In [4], the gain selection was derived assuming fast flux-estimation dynamics. In the case of SyRMs, the flux-estimation dynamics cannot be typically omitted. Instead, the speed-tracking loop (10) has to be tuned for a high bandwidth (approximately ten times that of the flux-estimation dynamics). Therefore, the tuning of the combined observer should be reconsidered for SyRMs.

IV. PROPOSED SCHEME

A. Cross-Saturation Compensation

Since the information provided by the signal-injection method corrects the internal states of the underlying full-order observer according to (24), the effect of the cross-saturation on the position error (22) should preferably be compensated for by directly correcting the error signal ϵ. The proposed method is to use a combination of the d and q axis current components, which is demodulated and low-pass filtered,

$$\epsilon = \mathrm{LPF}\left\{\left(\frac{\hat{L}_{\mathrm{dq}}}{\hat{L}_{\mathrm{qq}}}i_{\mathrm{d}} + i_{\mathrm{q}}\right)\sin(\omega_{\mathrm{c}}t)\right\} \tag{29}$$

where $\hat{L}_{\mathrm{dq}}$ and $\hat{L}_{\mathrm{qq}}$ are the model incremental inductances. This demodulation process is depicted in Fig. 3(b). The ratio $\hat{L}_{\mathrm{dq}}/\hat{L}_{\mathrm{qq}}$ can be regarded as a compensation factor, which can also include other model and implementation uncertainties. It can be seen from Fig. 1(c) that $\hat{L}_{\mathrm{dq}}/\hat{L}_{\mathrm{qq}} > 0$, if $i_{\mathrm{q}} < 0$ and $\hat{L}_{\mathrm{dq}}/\hat{L}_{\mathrm{qq}} < 0$, if $i_{\mathrm{q}} > 0$.

Based on (18) and (29), the quasi-steady-state error signal ϵ is approximated as

$$\begin{aligned}
\epsilon \approx &\frac{u_{\mathrm{c}}}{2\omega_{\mathrm{c}}L_{\mathrm{det}}\hat{L}_{\mathrm{qq}}}\left(L_{\Delta}\hat{L}_{\mathrm{qq}} - L_{\mathrm{dq}}\hat{L}_{\mathrm{dq}}\right)\sin(2\tilde{\vartheta}_{\mathrm{m}}) \\
&-\frac{u_{\mathrm{c}}}{2\omega_{\mathrm{c}}L_{\mathrm{det}}\hat{L}_{\mathrm{qq}}}\left(L_{\Delta}\hat{L}_{\mathrm{dq}} + L_{\mathrm{dq}}\hat{L}_{\mathrm{qq}}\right)\cos(2\tilde{\vartheta}_{\mathrm{m}}) \\
&+\frac{u_{\mathrm{c}}}{2\omega_{\mathrm{c}}L_{\mathrm{det}}\hat{L}_{\mathrm{qq}}}\left(L_{\Delta}\hat{L}_{\mathrm{dq}} + \hat{L}_{\mathrm{dq}}L_{\mathrm{qq}}\right).
\end{aligned} \tag{30}$$

Assuming accurate model parameters and small position error, this error signal reduces to

$$\epsilon \approx \frac{u_{\mathrm{c}}}{\omega_{\mathrm{c}}}\frac{L_{\Delta}L_{\mathrm{qq}} - L_{\mathrm{dq}}^2}{L_{\mathrm{det}}L_{\mathrm{qq}}}\tilde{\vartheta}_{\mathrm{m}} \tag{31}$$

which vanishes with $\tilde{\vartheta}_{\mathrm{m}} = 0$. Hence, the position error caused by the cross-saturation can be ideally reduced to zero if the ratio $\hat{L}_{\mathrm{dq}}/\hat{L}_{\mathrm{qq}}$ is known.

This method is closely related to the method proposed in [2], which is based on tracking the flux variations in the estimated q-axis direction. However, the scheme in [2] requires relatively high-amplitude carrier voltage signal and the stability analysis of the method has been omitted.

B. Observer Gain Selection

Because the correction signal ω_{ϵ} in (24) affects the dynamics of the underlying full-order observer, the observer gains defined by (12) do not guarantee the stability of the augmented system and tuning of the combined observer has to be reconsidered. Since signal injection is applied only at the lowest speeds, the transition between the gains in (12) and the modified gains should be seamless.

The effect of different gain selections on the stability of the combined observer was analyzed using the linearized estimation-error dynamics given in the Appendix. Numerical studies indicated that the gain selection (12) with $b > 0$ and $c > 0$ does not guarantee the stability of the combined observer at very low speeds. However, this instability due to

the interaction between the adaptive observer and the signal-injection correction can be remedied with the modified gains,

$$k_{11} = k'_{11} - k_1 f(\hat{\omega}_{\mathrm{m}}) \tag{32a}$$
$$k_{12} = -\beta k_{11} \tag{32b}$$
$$k_{21} = k'_{21} + k_2\beta f(\hat{\omega}_{\mathrm{m}}) \tag{32c}$$
$$k_{22} = -\beta k_{21} \tag{32d}$$

where k_1 and k_2 are positive constants and the function f is given in (28). It can be seen that these gains reduce to those given in (12) at higher speeds, when the signal-injection method is disabled.

The modified gains (32) can be also interpreted as replacing the observer parameters b and $c/\hat{\omega}_{\mathrm{m}}$ in (13) with

$$b_1 = b + (k_2\beta^2 + k_1)f(\hat{\omega}_{\mathrm{m}}) \tag{33a}$$
$$c_1 = \frac{c}{\hat{\omega}_{\mathrm{m}}} + \beta(k_1 - k_2)f(\hat{\omega}_{\mathrm{m}}), \tag{33b}$$

respectively, which now are not necessarily positive. It can be seen that the sign of c_1 can be either positive or negative, while b_1 remains positive.

The robustness of the combined observer is studied using the linearized estimation-error dynamics given in the Appendix. The standstill operation with the negative and positive rated loads was considered. The actual parameters correspond to those of the 6.7-kW SyRM: $L_{\mathrm{d}} = 2.00$ p.u., $L_{\mathrm{q}} = 0.3$ p.u., and $R_{\mathrm{s}} = 0.042$ p.u. Tuning parameters are: $\rho = 2$ p.u., $u_{\mathrm{c0}} = 0.1$ p.u., $\omega_{\mathrm{c}} = 2\pi\cdot500$ rad/s, $\omega_{\Delta} = 0.1$ p.u., and $\alpha_{\mathrm{i0}} = 0.1$ p.u. The same relative uncertainty (10%) is assumed for all three model parameters $\hat{L}_{\mathrm{d}}$, $\hat{L}_{\mathrm{q}}$, and $\hat{R}_{\mathrm{s}}$. Hence, eight different worst-case combinations, consisting of minimum and maximum values of the model parameters, can be formed. For example, one of the worst-case combinations is $\hat{L}_{\mathrm{d}} = 0.9L_{\mathrm{d}}$, $\hat{L}_{\mathrm{q}} = 1.1L_{\mathrm{q}}$, and $\hat{R}_{\mathrm{s}} = 0.9R_{\mathrm{s}}$. At each studied operating point, the local stability of the system was analyzed for all eight worst-case combinations of erroneous model parameters.

The stability of the estimation-error dynamics with erroneous model parameters was tested for different values of the design parameters b and c_1. The stability maps are depicted in Fig. 4, where stable areas are shaded and unstable areas are blank. Fig. 4(a) and Fig. 4(b) show the stability maps in the design-parameter space for $i_{\mathrm{q}} = -0.9$ p.u. and for $i_{\mathrm{q}} = 0.9$ p.u., respectively. It can be seen that the shape of the stable region changes with varying load, and that there are no stable points for $c_1 > 0$, when $i_{\mathrm{q}} = -0.9$ p.u. for this particular case. It is worth noticing that the combined observer is more robust when applied for PMSM drives, since the stability is governed by the operation-point parameter β, which for PMSMs is [18]

$$\beta = \frac{(L_{\mathrm{d}} - L_{\mathrm{q}})i_{\mathrm{q}}}{\psi_{\mathrm{pm}} + (L_{\mathrm{d}} - L_{\mathrm{q}})i_{\mathrm{d}}}$$

where ψ_{pm} is the permanent-magnet flux. For PMSMs, the parameter β does not change as drastically as it does for SYRMs when the load changes.

V. EXPERIMENTAL SETUP AND PARAMETERS

The motion-sensorless control system was implemented in a dSPACE DS1104 PPC/DSP board. A 6.7-kW four-pole SyRM
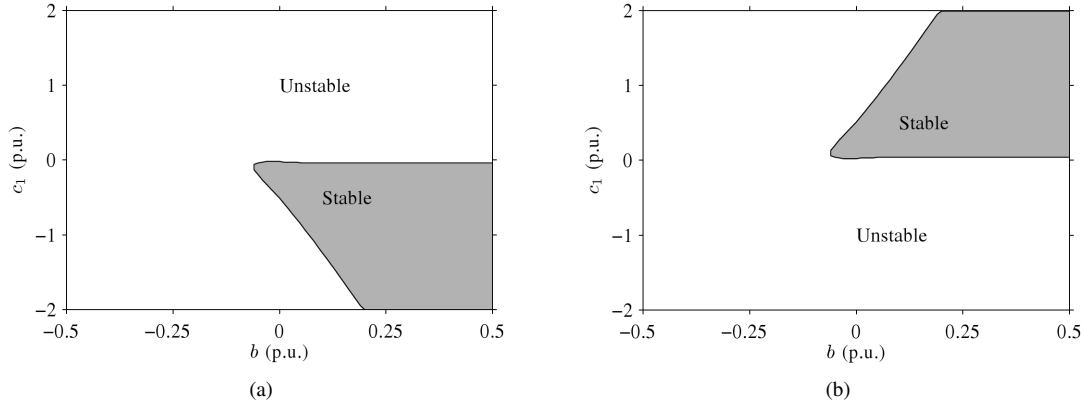
Fig. 4. Stability maps in the design parameter space for 10% parameter uncertainties: (a) $i_q = -0.9$ p.u., and (b) $i_q = 0.9$ p.u. The d-axis current is $i_d = 0.45$ p.u. and $\hat{\omega}_m = 0$. Stable areas are shaded and unstable areas are blank.
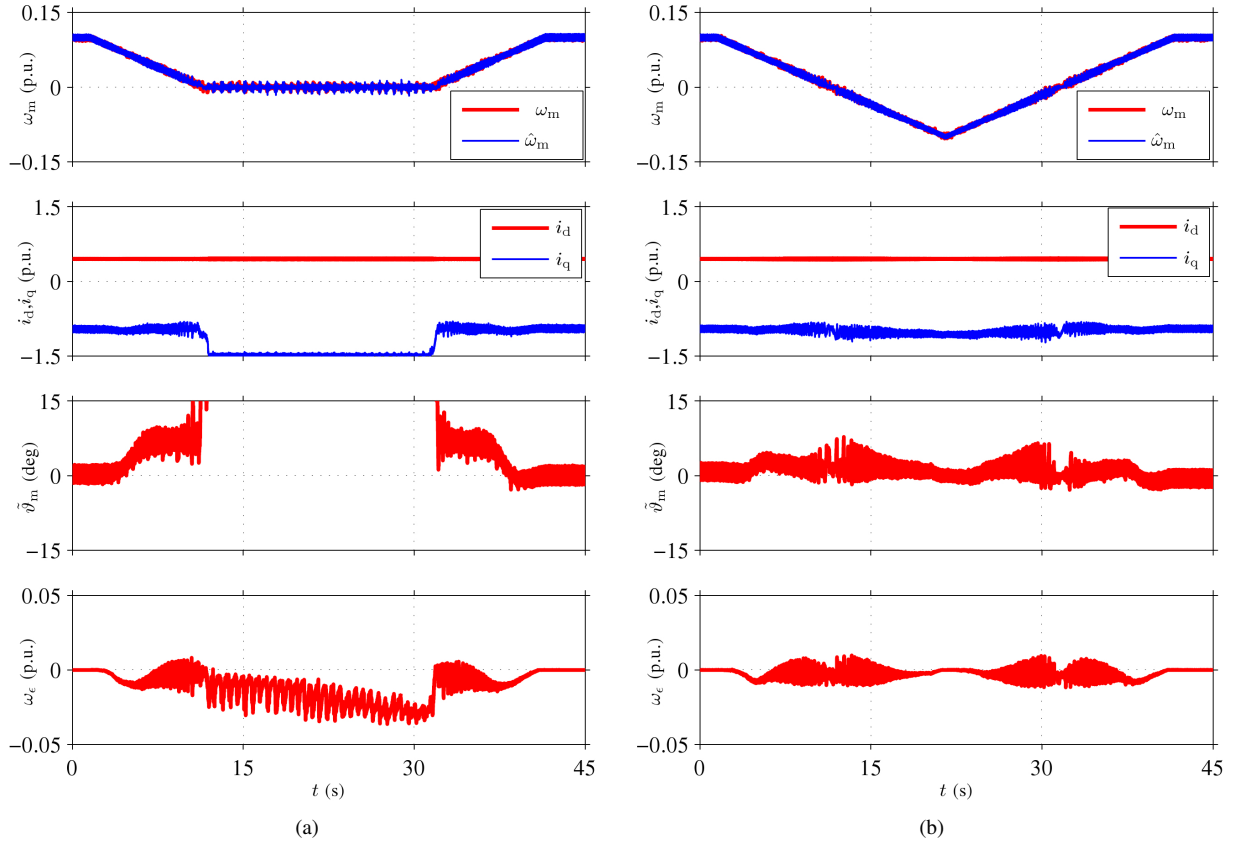

Fig. 5. Experimental results of a sloped speed reversal (0.1 p.u. $\rightarrow$ -0.1 p.u. $\rightarrow$ 0.1 p.u.) with negative rated load torque applied. The d-axis current is 0.45 p.u., and the compensation for the cross saturation is: (a) $\hat{L}_{dq}/\hat{L}_{qq} = 0$, (b) $\hat{L}_{dq}/\hat{L}_{qq} = -0.45 \cdot \frac{2}{\pi} \arctan{(i_q/0.2 \text{ p.u.})}$.

was fed by a frequency converter that is controlled by the DS1104 board. The rated values of the SyRM are: speed 3175 r/min; frequency 105.8 Hz; line-to-line rms voltage 370 V; rms current 15.5 A; and torque 20.1 Nm. The base values for angular speed, voltage, and current are defined as $2\pi \cdot 105.8$ rad/s, $\sqrt{2/3} \cdot 370$ V, and $\sqrt{2} \cdot 15.5$ A, respectively.

A servo motor was used as a loading machine. The rotor speed ω_m and position ϑ_m were measured using an incremental encoder for monitoring purposes. The total moment of inertia of the experimental setup is 0.015 kgm^2 (2.7 times the inertia of the SyRM rotor).

The stator currents and the DC-link voltage were measured, and the reference voltage obtained from the current controller was used for the observer. The sampling was synchronized to the modulation, and both the switching frequency and the sampling frequency were 5 kHz. A simple current feedforward compensation for dead times and power device voltage drops was applied.

The control system was augmented with a speed controller, whose feedback signal was the speed estimate $\hat{\omega}_m$ obtained

TABLE I
PER-UNIT PARAMETERS FOR SATURATION MODEL

L_{du}	L_{qu}	α	γ	δ	k	l	m	n
2.73	0.843	0.333	5.58	2.60	6.6	0.8	1	0
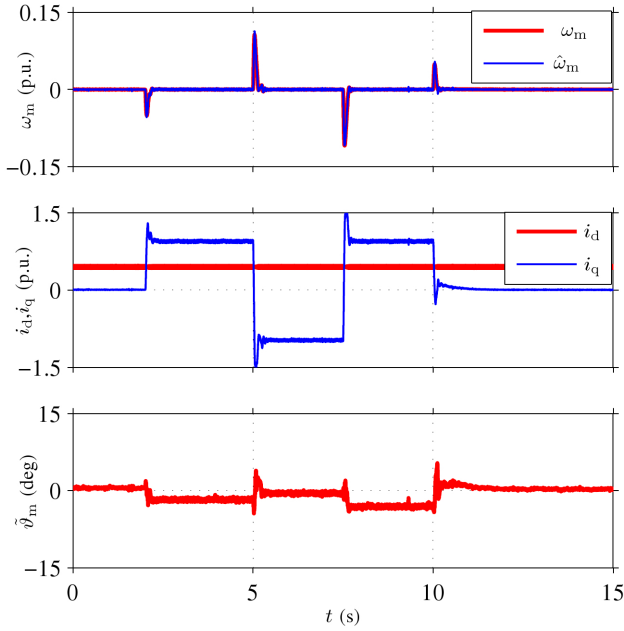
Fig. 6. Experimental results showing load-torque steps ($0 \rightarrow$ rated $\rightarrow -$ rated $\rightarrow$ rated $\rightarrow 0$) when the speed reference is kept at 0. The d-axis current is 0.45 p.u.

Fig. 7. Experimental results showing load-torque reversal (rated $\rightarrow -$ rated) when the SyRM drive is operated in the torque-control mode. The d-axis current is 0.45 p.u. The speed reference of the loading machine is kept at 0.

from the proposed observer. The bandwidth of this PI controller, including active damping [24], was 0.05 p.u. The gain values were chosen based on empirical results: $b = 0.05$, $c = 0.1\hat{\omega}_m^2/\omega_\Delta$, $k_1 = 0.075$, $k_2 = 0.025$, and $\rho = 2$ p.u. The parameters for the signal injection were: $u_{c0} = 0.1$ p.u., $\omega_c = 2\pi \cdot 500$ rad/s, $\omega_\Delta = 0.1$ p.u., and $\alpha_{i0} = 0.1$ p.u. The model stator resistance is $\hat{R}_s = 0.045$ p.u. The saturation model parameters are given in Table I [19]. Since at low speeds even small model parameter errors may result in considerable errors in the estimated fluxes, the saturation model is implemented using the measured current components as independent variables. Then, another estimates for $\hat{\psi}_d$ and $\hat{\psi}_q$ are searched iteratively so that the estimation errors $\hat{i}_d - i_d$ and $\hat{i}_q - i_q$ vanish. Unless otherwise mentioned, the compensation for cross saturation is modeled as

$$\frac{\hat{L}_{dq}}{\hat{L}_{qq}} = -0.45 \cdot \frac{2}{\pi} \arctan\left(\frac{i_q}{0.2 \text{ p.u.}}\right). \qquad (34)$$

VI. EXPERIMENTAL RESULTS

Experimental results of a sloped speed reversal from $\hat{\omega}_m = 0.1$ p.u. to $\hat{\omega}_m = -0.1$ p.u. and back to 0.1 p.u. with negative rated load torque applied using only the q-axis component of the high-frequency current ($\hat{L}_{dq}/\hat{L}_{qq} = 0$) are depicted in Fig. 5(a). It can be seen that the system is unstable and fails to cross the zero speed due to large position error.
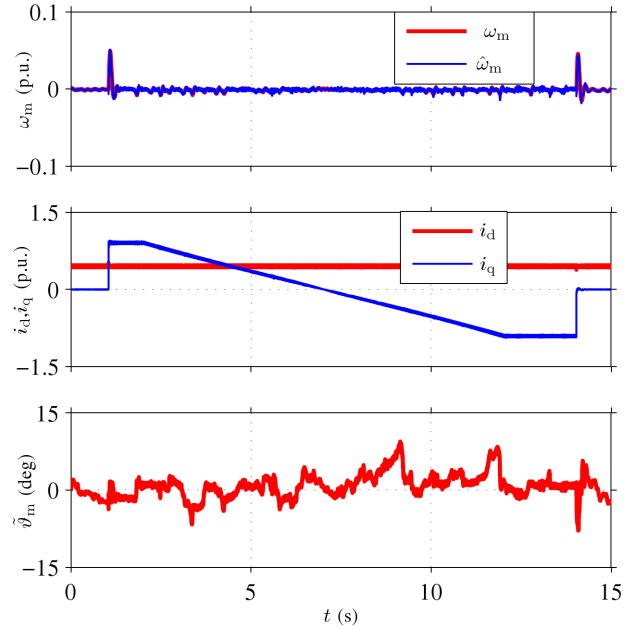
Similar results with the proposed cross-saturation compensation method are depicted in Fig. 5(b). It can be seen that the mean position error is close to zero and the noise in the estimation error is smaller. Experiments indicated that the drive becomes unstable in this particular test if the error in $\hat{R}_s$ is larger than approximately $\pm 10\%$.

Experimental results of load-torque steps when the speed reference was kept at 0 are shown in Fig. 6. The load torque was stepped to the rated load torque at $t = 2.0$ s, reversed at $t = 5.0$ s, reversed again at $t = 7.5$ s and removed at $t = 10$ s. It can be seen that the combined observer behaves well in load transients in standstill operation.

Experimental results of sloped torque reversal when the speed reference of the loading machine was kept at 0 are shown in Fig. 7. The SyRM drive is operated in the torque-control mode. It can be seen that the combined observer behaves well in this experiment. There is a region at $t \approx 9.0$ s near no-load condition where the cross saturation is not properly compensated by the simple compensation function (34). This modeling error can also be seen in Fig. 1(c), where L_{dq} increases rapidly as function of i_q in the vicinity of $i_q = 0$.

VII. CONCLUSIONS

In this paper, an adaptive full-order observer with signal injection is implemented and improved for SyRM drives. The evaluated scheme demonstrates good performance and small position error in laboratory experiments, but is relatively sensitive to the parameter errors of the fundamental-excitation model. This suggests that the scheme could be further improved with a stator-resistance adaptation mechanism, for example.

$$\frac{\mathrm{d}}{\mathrm{d}t}\begin{bmatrix} \tilde{\psi}_{\mathrm{d}} \\ \tilde{\psi}_{\mathrm{q}} \\ \tilde{\vartheta}_{\mathrm{m}} \\ \tilde{\omega}_{\mathrm{m}} \\ \tilde{\omega}_{\epsilon} \\ \tilde{\epsilon} \end{bmatrix} = \begin{bmatrix} k_{11} & g_{12} & g_{13} & \tilde{\psi}_{\mathrm{q}0} & \tilde{\psi}_{\mathrm{q}0} + L_{\mathrm{q}}i_{\mathrm{q}} & 0 \\ g_{21} & k_{22} & g_{23} & -\tilde{\psi}_{\mathrm{d}0} & -\tilde{\psi}_{\mathrm{d}0} - L_{\mathrm{d}}i_{\mathrm{d}} & 0 \\ 0 & 0 & 0 & 1 & 0 & 0 \\ g_{41} & g_{42} & g_{43} & g_{44} & g_{45} & 0 \\ 0 & 0 & \gamma_{\mathrm{p}}\alpha_{\mathrm{lp}}k_{\epsilon} & 0 & 0 & \gamma_{\mathrm{i}} - \gamma_{\mathrm{p}}\alpha_{\mathrm{lp}} \\ 0 & 0 & \alpha_{\mathrm{lp}}k_{\epsilon} & 0 & 0 & -\alpha_{\mathrm{lp}} \end{bmatrix} \begin{bmatrix} \tilde{\psi}_{\mathrm{d}} \\ \tilde{\psi}_{\mathrm{q}} \\ \tilde{\vartheta}_{\mathrm{m}} \\ \tilde{\omega}_{\mathrm{m}} \\ \tilde{\omega}_{\epsilon} \\ \tilde{\epsilon} \end{bmatrix} \tag{36}$$

APPENDIX
LINEARIZED ESTIMATION-ERROR DYNAMICS

It is assumed that zero position error is obtained in the operating point. The dynamics of the first-order low-pass filter of the demodulation process is modeled as

$$\frac{\mathrm{d}\tilde{\epsilon}}{\mathrm{d}t} = \alpha_{\mathrm{lp}}(k_{\epsilon}\tilde{\vartheta}_{\mathrm{m}} - \tilde{\epsilon}) \tag{35}$$

where the tilde refers to the small-signal quantities. The linearized closed-loop system consisting of (1) – (4), (8) – (11), (23), (24), (31), and (35) is expressed in (36), where

$$g_{12} = k_{12} + \omega_{\mathrm{m}0} + \omega_{\epsilon0}$$
$$g_{13} = -(k_{12} + \beta k_{11} + \omega_{\epsilon0})(L_{\mathrm{d}} - L_{\mathrm{q}})i_{\mathrm{d}}$$
$$g_{21} = k_{21} - \omega_{\mathrm{m}0} - \omega_{\epsilon0}$$
$$g_{23} = -(k_{22} + \beta k_{21} - \beta\omega_{\epsilon0})(L_{\mathrm{d}} - L_{\mathrm{q}})i_{\mathrm{d}}$$
$$g_{41} = d\frac{k_{21} - \omega_{\mathrm{m}0} - \omega_{\epsilon0}}{(\hat{L}_{\mathrm{d}} - \hat{L}_{\mathrm{q}})i_{\mathrm{d}}}$$
$$g_{42} = \frac{e + k_{22}d}{(\hat{L}_{\mathrm{d}} - \hat{L}_{\mathrm{q}})i_{\mathrm{d}}}$$
$$g_{43} = -\frac{L_{\mathrm{d}} - L_{\mathrm{q}}}{\hat{L}_{\mathrm{d}} - \hat{L}_{\mathrm{q}}}[e + d(k_{22} + \beta k_{21} - \beta\omega_{\epsilon0})]$$
$$g_{44} = -d\frac{\tilde{\psi}_{\mathrm{d}0} + (L_{\mathrm{d}} - L_{\mathrm{q}})i_{\mathrm{d}}}{(\hat{L}_{\mathrm{d}} - \hat{L}_{\mathrm{q}})i_{\mathrm{d}}}$$
$$g_{45} = -d\frac{\tilde{\psi}_{\mathrm{d}0} + L_{\mathrm{d}}i_{\mathrm{d}}}{(\hat{L}_{\mathrm{d}} - \hat{L}_{\mathrm{q}})i_{\mathrm{d}}}.$$

The steady-state error of the q-axis flux is $\tilde{\psi}_{\mathrm{q}0} = (\hat{L}_{\mathrm{q}} - L_{\mathrm{q}})\beta i_{\mathrm{d}}$, and $\tilde{\psi}_{\mathrm{d}0}$ and $\omega_{\epsilon0}$ can be solved from

$$\tilde{\psi}_{\mathrm{d}0}k_{11} + i_{\mathrm{d}}(\hat{L}_{\mathrm{q}} - L_{\mathrm{q}})\beta\omega_{\mathrm{m}0}$$
$$+ i_{\mathrm{d}}\left[(L_{\mathrm{d}} - \hat{L}_{\mathrm{d}})k_{11} - \tilde{R}_{\mathrm{s}} + \hat{L}_{\mathrm{q}}\beta\omega_{\epsilon0}\right] = 0 \tag{37a}$$
$$i_{\mathrm{d}}k_{21}(L_{\mathrm{d}} - \hat{L}_{\mathrm{d}}) - \tilde{R}_{\mathrm{s}}\beta i_{\mathrm{d}} - L_{\mathrm{d}}i_{\mathrm{d}}\omega_{\epsilon0}$$
$$- \tilde{\psi}_{\mathrm{d}0}(\omega_{\epsilon0} - k_{21} + \omega_{\mathrm{m}0}) = 0 \tag{37b}$$

The local stability of the combined observer can be analyzed using these relations.

REFERENCES

[1] R. Lagerquist, I. Boldea, and J. Miller, "Sensorless control of the synchronous reluctance motor," *IEEE Trans. Ind. Appl.*, vol. 30, no. 3, pp. 673–682, May/June 1994.

[2] E. Capecchi, P. Guglielmo, M. Pastorelli, and A. Vagati, "Position-sensorless control of the transverse-laminated synchronous reluctance motor," *IEEE Trans. Ind. Appl.*, vol. 37, no. 6, pp. 1768–1776, Nov./Dec. 2001.

[3] H. F. Hofmann, S. R. Sanders, and A. EL-Antably, "Stator-flux-oriented vector control of synchronous reluctance machines with maximized efficiency," *IEEE Trans. Ind. Electron.*, vol. 51, no. 5, pp. 1066–1072, Oct. 2004.

[4] A. Piippo, M. Hinkkanen, and J. Luomi, "Analysis of an adaptive observer for sensorless control of interior permanent magnet synchronous motors," *IEEE Trans. Ind. Electron.*, vol. 55, no. 2, pp. 570–576, Feb. 2008.

[5] M. Hinkkanen, T. Tuovinen, L. Harnefors, and J. Luomi, "A combined position and stator-resistance observer for salient PMSM drives: design and stability analysis," *IEEE Trans. Power Electron.*, vol. 27, no. 2, pp. 601–609, Feb. 2012.

[6] J.-I. Ha, S.-J. Kang, and S.-K. Sul, "Position-controlled synchronous reluctance motor without rotational transducer," *IEEE Trans. Ind. Appl.*, vol. 35, no. 6, pp. 1393–1398, Nov./Dec. 1999.

[7] A. Consoli, F. Russo, G. Scarcella, and A. Testa, "Low- and zero-speed sensorless control of synchronous reluctance motors," *IEEE Trans. Ind. Appl.*, vol. 35, no. 5, pp. 1050–1057, Sep./Oct. 1999.

[8] H. W. de Kock, M. J. Kamper, O. C. Ferreira, and R. M. Kennel, "Position sensorless control of the reluctance synchronous machine considering high frequency inductances," in *Proc. PEDS 2007*, Bangkok, Thailand, Nov. 2007, pp. 812–821.

[9] S.-C. Agarlită, I. Boldea, and F. Blaabjerg, "High-frequency-injection-assisted "active flux"-based sensorless vector control of reluctance synchronous motors, with experiments from zero speed," *IEEE Trans. Ind. Appl.*, vol. 48, no. 6, pp. 1931–1939, Nov./Dec. 2012.

[10] M. Schroedl and P. Weinmeier, "Sensorless control of reluctance machines at arbitrary operating conditions including standstill," *IEEE Trans. Power Electron.*, vol. 9, no. 2, pp. 225–231, Mar. 1994.

[11] R. Morales-Caporal and M. Pacas, "Encoderless predictive direct torque control for synchronous reluctance machines at very low and zero speed," *IEEE Trans. Ind. Electron.*, vol. 55, no. 12, pp. 4408–4416, Dec. 2008.

[12] T. Matsuo and T. A. Lipo, "Rotor position detection scheme for synchronous reluctance motor based on current measurements," *IEEE Trans. Ind. Appl.*, vol. 31, no. 4, pp. 860–868, July/Aug. 1995.

[13] M.-Y. Wei and T.-H. Liu, "A high-performance sensorless position control system of a synchronous reluctance motor using dual current-slope estimating technique," *IEEE Trans. Ind. Electron.*, vol. 59, no. 9, pp. 3411–3426, Sept. 2012.

[14] M. J. Corley and R. D. Lorenz, "Rotor position and velocity estimation for a salient-pole permanent magnet synchronous machine at standstill and high speeds," *IEEE Trans. Ind. Appl.*, vol. 34, no. 4, pp. 784–789, Jul./Aug. 1998.

[15] O. Wallmark, L. Harnefors, and O. Carlson, "An improved speed and position estimator for salient permanent-magnet synchronous motors," *IEEE Trans. Ind. Electron.*, vol. 52, no. 1, pp. 255–262, Feb. 2005.

[16] W. Hammel and R. M. Kennel, "Position sensorless control of PMSM by synchronous injection and demodulation of alternating carrier voltage," in *Proc. IEEE SLED 2010*, Padova, Italy, July 2010, pp. 56–63.

[17] W. T. Villet, M. J. Kamper, P. Landsmann, and R. Kennel, "Hybrid position sensorless vector control of a reluctance synchronous machine through the entire speed range," in *Proc. EPE-PEMC'12*, vol. 1, Novi Sad, Serbia, Sept. 2012, pp. 1–7.

[18] T. Tuovinen, M. Hinkkanen, L. Harnefors, and J. Luomi, "Comparison of a reduced-order observer and a full-order observer for sensorless synchronous motor drives," *IEEE Trans. Ind. Appl.*, vol. 48, no. 6, pp. 1959–1967, Nov./Dec. 2012.

[19] Z. Qu, T. Tuovinen, and M. Hinkkanen, "Inclusion of magnetic saturation in dynamic models of synchronous reluctance motors," in *Proc. ICEM'12*, Marseille, France, Sept. 2012, pp. 994–1000.

[20] G. Yang, R. Tomioka, M. Nakano, and T. H. Chin, "Position and speed sensorless control of brushless DC motor based on an adaptive observer," *IEEJ Trans. Ind. Appl.*, vol. 113, pp. 579–586, May 1993.

[21] L. Harnefors and H.-P. Nee, "A general algorithm for speed and position estimation of AC motors," *IEEE Trans. Ind. Electron.*, vol. 47, no. 1, pp. 77–83, Feb. 2000.

[22] W. T. Villet, M. J. Kamper, P. Landsmann, and R. Kennel, "Evaluation of a simplified high frequency injection position sensorless control method for reluctance synchronous machine drives," in *Proc. IET PEMD 2012*, vol. 1, Bristol, UK, Mar. 2012, pp. 1–6.

[23] P. Guglielmi, M. Pastorelli, and A. Vagati, "Impact of cross-saturation in sensorless control of transverse-laminated synchronous reluctance motors," *IEEE Trans. Ind. Electron.*, vol. 53, no. 2, pp. 429–439, Apr. 2006.

[24] L. Harnefors, "Design and analysis of general rotor-flux-oriented vector control systems," *IEEE Trans. Ind. Electron.*, vol. 48, no. 2, pp. 383–390, Apr. 2001.

Marko Hinkkanen (M'06–SM'13) received the M.Sc.(Eng.) and D.Sc.(Tech.) degrees from Helsinki University of Technology, Espoo, Finland, in 2000 and 2004, respectively.

Since 2000, he has been with Helsinki University of Technology (part of Aalto University, Espoo, since 2010). He is currently an Assistant Professor with the Department of Electrical Engineering, Aalto University. His research interests include electric drives and electric machines.

Toni Tuovinen received the M.Sc. degree from University of Helsinki, Helsinki, Finland, in 2005, and the M.Sc.(Eng.) degree from Helsinki University of Technology, Espoo, Finland, in 2009.

Since 2007, he has been with Helsinki University of Technology (part of Aalto University, Espoo, since 2010). He is currently a Research Scientist with the Department of Electrical Engineering, Aalto University. His main research interest is the control of electric drives.